Full Length Article

Structural, chemical and electrical characterisation of conductive graphene-polymer composite films

Barry Brennan [a], Steve J. Spencer [a], Natalie A. Belsey [a], Tsegie Faris [b], Harry Cronin [b,c], S. Ravi P. Silva [c], Toby Sainsbury [a], Ian S. Gilmore [a], Zlatka Stoeva [b], Andrew J. Pollard [a,*]

[a] National Physical Laboratory, Teddington, TW11 0LW, United Kingdom
[b] DZP Technologies Ltd., Future Business Centre, Cambridge, CB4 2HY, United Kingdom
[c] Advanced Technology Institute (ATI), University of Surrey, Guildford, GU2 7XH, United Kingdom

ABSTRACT

Graphene poly-acrylic and PEDOT:PSS nanocomposite films were produced using two alternative commercial graphene powders to explore how the graphene flake dimensions and chemical composition affected the electrical performance of the film. A range of analytical techniques, including scanning electron microscopy (SEM), atomic force microscopy (AFM), Raman spectroscopy, X-ray photoelectron spectroscopy (XPS) and time-of-flight secondary ion mass spectrometry (ToF-SIMS), were employed to systematically analyse the initial graphene materials as well as the nanocomposite films. Electrical measurements indicated that the sheet resistance of the films was affected by the properties of the graphene flakes used. To further explore the composition of the films, ToF-SIMS mapping was employed and provided a direct means to elucidate the nature of the graphene dispersion in the films and to correlate this with the electrical analysis. These results reveal important implications for how the dispersion of the graphene material in films produced from printable inks can be affected by the type of graphene powder used and the corresponding effect on electrical performance of the nanocomposites. This work provides direct evidence for how accurate and comparable characterisation of the graphene material is required for real-world graphene materials to develop graphene enabled films and proposes a measurement protocol for comparing graphene materials that can be used for international standardisation.

Crown Copyright © 2017 Published by Elsevier B.V. All rights reserved.

1. Introduction

Next generation consumer electronic devices are predicted to be built around a platform which relies on increased integration of technologies into everyday life, providing seamless interfacing between smart devices, the user, and the environment in which they operate [1,2]. In order to realise this, more adaptable devices are needed, which provide increased functionality and are not limited to the form factors associated with traditional silicon based technology, and yet do not suffer any significant decrease in performance relative to current technologies [3,4]. Cheaper, lightweight, flexible materials are therefore required to enable this technological revolution. This is a key reason why graphene and related 2D materials have garnered much attention since their discovery several years ago [5–8]. Due to its extremely promising electrical, mechanical and thermal characteristics, graphene

is currently under investigation for use in many different application areas, such as sensors [9], mechanical reinforcement [10], energy storage [11–13], energy capture [14,15], barrier layers [16], and as the active material in a number of different device architectures [17–19]. Specifically, its potential application as a conductive material, due to its exceptional electron mobility, has large-scale, near-term commercial potential [20,21]. Coupled with its optical transparency, graphene is a suitable candidate to replace indium tin oxide (ITO) as the transparent conductor of choice for consumer electronics [22]. ITO, while having excellent conductivity and transparency characteristics, suffers from poor mechanical flexibility, requires a high annealing temperature, is relatively expensive and is prone to market instability on cost and supply [23]. Graphene on the other hand is flexible, can be easily printed [24] and, due to continued refinement of the production process, continues to decrease in cost. The potential for formation of high quality synthetic graphite source material in the near future means supply should not be an issue [25].

However, there are obstacles still to overcome with graphene before it is ready for use in commercial applications and can

compete with ITO on performance and stability. Issues with the consistency of graphene materials [26,27], variations in the composition between suppliers and production methods [28], even the definition of what can be described as graphene must all be addressed [29].[1]

Chemical vapour deposition (CVD) production of graphene, while now able to produce large area sheets, is still prone to a level of defects and grain boundaries which impact on the material properties [15,30–33]. Liquid-phase exfoliated graphene powders or dispersions, while technically able to produce more pristine graphene flakes, are still liable to have issues due to contamination coming from the source graphite material and surfactants used to keep the graphene stable in a dispersion [34,35]. Also, the significant variation in flake lateral size and thickness observed in the shearing process to form graphene/graphite dispersions can lead to difficulties in producing repeatable properties of printed graphene films [36]. In order to utilise graphene powders in printable inks that can produce conductive films, it is generally necessary to embed the graphene in a binder material [5,12,24,37]. These binders can already have conductive properties, such as poly(3,4-ethylenedioxythiophene):poly(styrenesulfonate) (PEDOT:PSS), with the graphene potentially acting to enhance the conductive properties and stability of the printed films. In the case of non-conductive binders, the distribution of graphene particles within the polymer matrix is crucial for achieving the desired conductive properties. Significant research has been performed in the area of incorporating graphene and graphene oxide flakes in conductive and dissipative polymer matrices [38–40]. However, while electrical measurements, that are standardised for conductive films in general, can be used to determine the conductivity of these printed graphene films, actually determining how the graphene is distributed in non-transparent printed films is less straightforward. This is due to the relative chemical inertness, high bond strength, low concentration in relation to the surrounding material and small dimensions of graphene. These factors limit what spectroscopic techniques can be used to identify the location and nature of the graphene that is present in the films.

Characterisation of dispersed graphene material, especially in a largely carbon matrix such as a polymer, can be difficult and requires a number of complementary approaches, as no one technique is currently able to fulfil all of the physical and chemical measurement requirements. Properties such as the size and thickness of graphene flakes and location within samples, chemical information regarding presence of contamination and binding environments, and levels of defects present are all critical to performance. For this reason, a range of measurement techniques are needed.

In this study, graphene films have been investigated using two different graphene source materials, with each introduced into two different polymer binders. Complementary characterisation techniques were employed to comprehensively characterise the graphene/graphite material itself; Raman spectroscopy, scanning electron microscopy (SEM), atomic force microscopy (AFM), X-ray photoelectron spectroscopy (XPS) and time-of-flight secondary ion mass spectrometry (ToF-SIMS). Then, using novel analysis procedures, ToF-SIMS was used to identify where the graphitic material was located in the films. This comprehensive understanding of the material and the dispersion of the graphene was compared to the electrical properties of the same films, to determine how the different properties of the source material affect the final desired characteristics of the films. The aim of this study was not

to pass judgement on the graphene used in these films, or to make the best performing graphene films from printable inks. Neither was this work to comment on the terminology used for the two commercially-available 'graphene'-labelled materials. Instead the aim was to systematically determine the differences where they exist, as it is likely that variations in the properties of the graphene material itself will have specific benefits or drawbacks depending on the desired application. This in turn highlights the need for adequate characterisation protocols and standards to aid the further development of graphene enabled devices and materials, by allowing the comparison of different graphene products produced via different processes. To this end, the characterisation procedure outlined here can be used as a basis for an international measurement standard, as currently being developed in ISO/TC229, within PWI 21356 'Nanotechnologies – Structural characterization of graphene'.

2. Experimental

2.1. Sample preparation

Carbon A and Carbon B were commercial graphene powder samples acquired from two suppliers, Thomas Swan and Co. Ltd (Elicarb® Graphene Powder) and Angstron Materials Inc. (N006-P) respectively. The Carbon A and Carbon B powders were then each dispersed in either a proprietary PMMA-based polymer binder developed at DZP Technologies Ltd. named 'MT46' or PEDOT:PSS in water, with a total graphene/graphite (i.e. carbon) powder content of 6.25% by weight in the case of MT46 polymer, and 2.00% by weight for the PEDOT:PSS samples. These printable inks were deposited on either polyethylene terephthalate (PET) transparent substrates for electrical measurements or aluminium foil for the XPS and ToF-SIMS measurements of the films, with the films having a final graphene powder content of 36% after drying in the case of MT46 binder, and 50% in the case of PEDOT:PSS. The quantities of graphene present in each sample were calculated on the basis of the quantities of raw materials used in each preparation. Separately, the carbon powders were also pressed into pellets and mounted on copper substrates using silver paint to allow for XPS, Raman spectroscopy and ToF-SIMS measurements of the source material.

After initial chemical characterisation, the pellets underwent a washing procedure, first being treated by bath sonication for 30 min (CamSonix C275T, Camlab, Cambridge, UK) in order to disperse the pellet into deionized water (250 mL). The carbon dispersion was then filtered using a membrane filtration apparatus (Millipore) in conjunction with an alumina filter membranes (Whatman, Anodisc, 0.2 μm pore size, 47 mm diameter) and was washed using an additional aliquot of deionised water (250 mL). The flakes collected on the filter membrane were then re-dispersed once again by sonication into deionised water (250 mL) (15 mins) and was filtered once more through the membrane filtration apparatus as mentioned above. This procedure was repeated once more in order to provide a rigorous washing procedure, and the material was subsequently re-analysed.

For SEM and AFM measurements, the original carbon powders were dispersed in isopropyl alcohol (5 mg mL^{-1}) and sonicated for 30 min. Samples were drop-cast (10 μL) onto 1×1 cm^2 native oxide or 300 nm oxide silicon wafer (University Wafer, Boston, MA, USA) for SEM and AFM measurements respectively. For initial SEM assessment of flake morphology the suspension was used neat. For SEM measurements of flake dimensions the dispersion was subject to a 100-fold dilution to generate sufficiently low-coverage to identify individual separated flakes. To produce these low-coverage samples for SEM, the substrate was heated to 60 °C prior to drop-casting which resulted in a more even flake distribu-

[1] Definition of the accepted terminology for graphene and related 2D materials is under development through the International Organization for Standardization (ISO) 'Nanotechnologies' Technical Committee (TC229).

tion with reduced agglomeration. The samples were subsequently heated in a vacuum oven at 35 °C for 12 h or more to remove as much residue on the wafer due to the dispersion as possible.

The films were cast from a printable ink onto pre-treated PET and Al substrates using a wire-wound rod coater, with a wire diameter of 3 mils (approximately 76 µm). This resulted in dry films of thickness of the order of 1 µm.

2.2. Characterisation of powders and films

For conductivity measurements, each film was cut into a fillet of 10×40 mm^2, and measured using a custom spring-loaded four-point probe attached to a Keithley 4200 SCS source-meter, with constant tip spacing of 3 mm. Sheet resistance values, in $\Omega/\square$, were calculated from the resistance data using a standard conversion formula. The thickness of each sample was determined by a focus variation method. The difference in height between the top and back surfaces of the samples was calculated based on the focal length of these surfaces when observed with an optical microscope. This was then combined with the measured sheet resistance of each fillet to yield resistivity, in units of Ω m, in order to account for the different thicknesses of the fillets, which can affect the sheet resistance measurement.

In order to determine the lateral distribution of flake sizes from the graphene/graphite powders, SEM was performed using a Zeiss (Oberkochen, Germany) Supra Microscope (In lens, 30 µm aperture, 5 kV accelerating voltage), with a minimum of 200 individual flakes measured to provide a statistically significant distribution measure of flake lateral size. The lateral size of each flake was determined by measuring the perpendicular length and width of the flakes and calculating the mean value of the two, via SmartTiff software, as shown in Fig. S1. Suitability of the sample preparation procedure for AFM analysis was first confirmed by SEM characterisation. AFM measurements were then performed, on a similarly prepared sample without SEM characterisation, using a Cypher S (Asylum Research, USA) system in 'tapping mode' with Pointprobe® NCHR cantilevers (NanoWorld, Switzerland) to measure the thickness of the flakes that were isolated on the wafer surface. The thickness was determined by analysing several horizontal profiles (that is, along the scanning axis), using SPIP™ software, as was the corresponding lateral size of each flake, using the same method as used for the SEM images. To determine the associated uncertainty for the thickness of each flake, several horizontal profiles (that is, along the scanning axis) of the flake were measured, using the point on the substrate next to the flake and the point at the apex of the increase in the topography due to the flake. The standard deviation in three values of thickness was used as the uncertainty, unless this was less than the RMS roughness of the substrate due to the height resolution of the instrument, the actual roughness of the substrate, or solvent residue; in which case the RMS roughness was used instead. The uncertainty in the lateral dimension for each flake was calculated from the slope of the edge of the flake, using the larger value of either the instrument lateral resolution or the uncertainty in where the edge of the flake was located. To provide a relevant set of data points, a range of flakes were selected for AFM investigation that corresponded to the range of lateral dimensions already determined for that graphene material using SEM.

Raman spectroscopy (LabRAM HR Evolution, Horiba Scientific, UK) was performed on pellets of carbon material using a 532 nm (2.33 eV) laser source and a 100×0.9NA lens, with a total laser spot power of less than 1 mW, and analysed using LabSpec 5 software. Ten spectra were taken from a pellet for each type of material to understand the variation across the sample. XPS measurements were then carried out using an Axis-Ultra (Kratos Analytical, UK) operating at a pass energy of 20 eV for high resolution, narrow scan window spectra (100 meV step size, 500 ms dwell time), and

160 eV for wide scans (1000 meV step size, 200 ms dwell time), using a monochromated Al Kα X-ray source, with a photon energy of 1486.7 eV. Spectra were taken from three individual areas of each sample, with and without charge neutralisation, using an electron flood gun to ensure effects of surface charging were accounted for. Spectral peak fitting was carried out using CasaXPS with Shirley type backgrounds for the high resolution spectra, and elemental composition calculated from the wide scans using the NPL transmission functions and average matrix relative sensitivity factors after removal of a Tougaard or linear background [41].

ToF-SIMS measurements of the carbon pellets and films were carried out on a TOF SIMS IV time-of-flight secondary ion mass spectrometer (ION-TOF GmbH, Germany), equipped with an argon cluster sputter gun and a liquid metal ion gun (LMIG) orientated at 45° to the sample surface. The LMIG utilised a Bi$_3^+$ ion source, operating at an ion current of 0.1 pA, raster scanned randomly in the defined region of interest to be imaged on the sample. 3D depth profiles were performed in a non-interlaced mode with sputtering cycles using 20 keV Ar$_{5000}$ gas clusters, at an ion current of 0.4 nA and cycle time of 200 µs, over an area of 400 µm × 400 µm, interleaved with secondary ion images generated by the LMIG over an area of 150 µm × 150 µm in the centre of the sputtered region. The smaller analysis region effectively gates the signal, reducing sputter crater edge effects on the quality of the spectra. An electron flood gun was also used to compensate for charging effects during the measurements, at an operating voltage of 20 eV. For the ToF-SIMS measurement of the films, a 10 mm × 10 mm sample was used.

3. Results and discussion

3.1. Electrical characterisation of films

Resistivity measurements from 6 different types of films are shown in Fig. 1. For each type of film the mean average of four measurements was calculated. When added to MT46, an insulating acrylic binder material, it is observed that Carbon B only reduced the resistivity by a small quantity; both samples acted as insulators within the measured configuration. In the case of the sample with Carbon A, there was a noticeable reduction in the resistivity, by approximately an order of magnitude, although the sample remained highly resistive. This decrease in the resistivity with the addition of Carbon A may be due to the formation of a percolation network [19], by having preferential pathways for the charge conduction, but still with very high resistance MT46 between each flake.

A similar effect for Carbon B was measured in the case of the PEDOT:PSS samples in Fig. 1(b), whereby the introduction of the graphene had little effect on the conductivity of the sample (within experimental errors). For Carbon A however, its introduction had a measurable negative effect on the conductivity of the samples. In this case (where PEDOT:PSS is a well-engineered conductive polymer) it suggests that the introduction of the graphene flakes could have a negative effect on the film forming properties of the PEDOT:PSS. From these measurements alone it is not possible to conclude as to the reason for this, but what is clear is that even if Carbon A is able to form a percolation network, there is still no increase in conductivity after its introduction. Previous work has also shown complex electronic couplings may develop between conjugate polymers and graphene [40].

While it would be easy to claim that one source of graphene is 'better' than the other, based on the results of the resistivity measurements, this would be too facile of a statement, as the true quality of the films depends on a number of factors. While sheet resistance may be an important parameter for some applications, other parameters may be beneficial for different applications. What
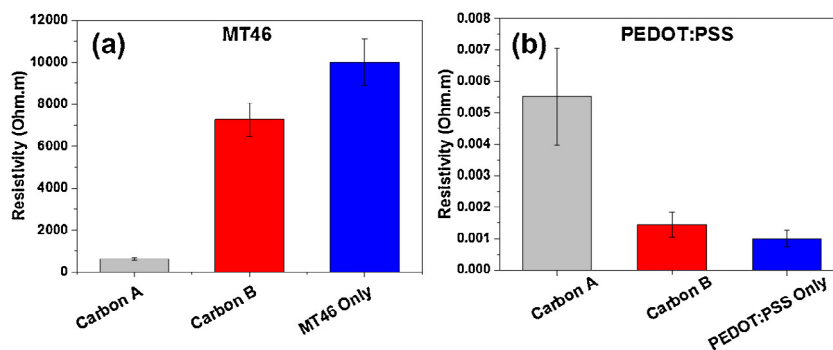
Fig. 1. Film resistivity: Resistivity measurements from Carbon A and Carbon B in (a) MT46 and (b) PEDOT:PSS, as well as graphene-free binder material controls, indicating a variation in resistivity depending on the graphene material used.

is clear is that the Carbon A and Carbon B produce differing electrical property results when added to these two polymer materials and to better understand the reasons for this, it is necessary to carry out detailed *material* characterisation of the graphene powders and the films themselves.

3.2. Structural characterisation of flakes

The current definition of 'graphene' refers to a single layer of carbon atoms with each atom bound to three neighbours in a honeycomb structure,[2] but in practice the term has been used much more loosely to represent any graphitic carbon material which has been produced in such a way to generate the thinnest layers or flakes of graphite possible. A typical production process for making graphene powders involves introducing natural graphite into either an organic solvent or an aqueous dispersion containing a surfactant, then a high graphite shearing rate system can be used to exfoliate the graphite flakes and reduce their thickness, separating out the individual layers of graphite [42]. Careful optimisation of the shearing process can lead to selectivity control of flake size and thickness. While transmission electron microscopy (TEM) may provide the highest resolution images of individual flakes, these measurements are very time consuming and rely on complicated sample preparation. For this reason, a combination of Raman spectroscopy, SEM and AFM can provide a faster and still reliable method of characterising the dimensional properties of a representative sample of the graphene flakes.

Raman spectra were acquired on pellets prepared from Carbon A and B, as shown in Fig. S2, revealing a graphitic carbon structure for both materials typical for bulk graphene/graphite powders. A sharp G-peak ($\sim$1580 cm^{-1}) and asymmetric 2D-peak ($\sim$2700 cm^{-1}) were observed in all areas, however, Carbon A had a consistently higher D-peak to G-peak intensity ratio ($I_D/I_G \approx 0.33$) than Carbon B ($I_D/I_G \approx 0.13$). Although a larger I_D/I_G value can be attributed to a greater level of disorder in graphene material [43–45], when performing a bulk measurement for graphene/graphite powders a larger I_D/I_G value may also be expected for a powder with a distribution of smaller flakes [46]. This is because the D-peak signal is observed when different types of defects in the graphitic lattice are present, such as the edge of a flake [47,48], thus a greater concentration of smaller flakes would mean a greater contribution due to edge defects.

The SEM images in Fig. 2, from (a) Carbon A and (b) Carbon B dispersions, indicate the significant variation in the lateral size of the graphitic flakes from the two sources, with a histogram of the lateral size distribution from 200 individual isolated flakes plotted

in (c). The measurements in (c) were acquired by performing a 100-fold dilution to the dispersions used to prepare the SEM images in Fig. 2, as shown in Fig. S1, to ensure measurements were only taken on isolated flakes. The images in (a) and (b) are scaled to have the same magnification, and it is clear that the flakes in the Carbon B dispersion are typically much larger in lateral size than those from the Carbon A dispersion, however, this increase in size appears to be at the expense of size uniformity, with a much greater range of sizes evident in the Carbon B material. The SEM images in Fig. 2 also qualitatively suggest that the flakes in Carbon B are much thicker than Carbon A. The quantitative relationship between flake thickness and lateral size is observed through AFM measurements, as shown in Fig. 3.

Flakes were observed with AFM that were similar in dimension to those present in the SEM images. Carbon B was found to have thicker flakes present than Carbon A, as shown in Fig. 3, with representative AFM images of isolated flakes shown in Fig. S3.

Typically, graphene or few-layer graphene flakes were present in both samples, with lateral dimensions up to several hundred nanometres. However, from the SEM analysis in Fig. 2(c), flakes of these lateral sizes were much more prevalent within Carbon A than Carbon B. Both samples revealed a trend of increasing thickness with lateral size, as expected, and is also observed for other 2D materials [49]. As Carbon B was found to have a larger lateral size distribution range, it can therefore be concluded from Fig. 3(a) that Carbon B had a much higher percentage of thicker flakes. Importantly the Raman spectroscopy, SEM, and AFM results all concur, showing consistently smaller flakes (lateral dimensions and thickness) for Carbon A, than Carbon B. This suggests that a larger concentration of smaller, thinner graphene flakes in Carbon A, leads to an increased conductivity in the MT46 non-conductive film, but this does not explain why it reduces the conductivity for the highly-conductive PEDOT:PSS film.

However, another feature that was consistently revealed in the AFM and Raman spectroscopy measurements from the Carbon A material was the presence of polymer-like residue on and around the graphitic material after dispersion. This was observed in the AFM measurements as a nanometre-scale surface height variation of the substrate that was reduced with heating within a vacuum oven, as well as unassigned peaks within the Raman spectra, shown in Fig. S2(c), suggesting non-graphitic chemical species were present.

3.3. Chemical characterisation

XPS measurements were also performed on the same pellets in order to determine the chemical composition of the materials. While sp^2 carbon-carbon bonding dominates the carbon XPS spectra from both samples, as shown in Fig. 4, based on the peak

---

[2] ISO TS 80004-3:2010, definition 2.11.
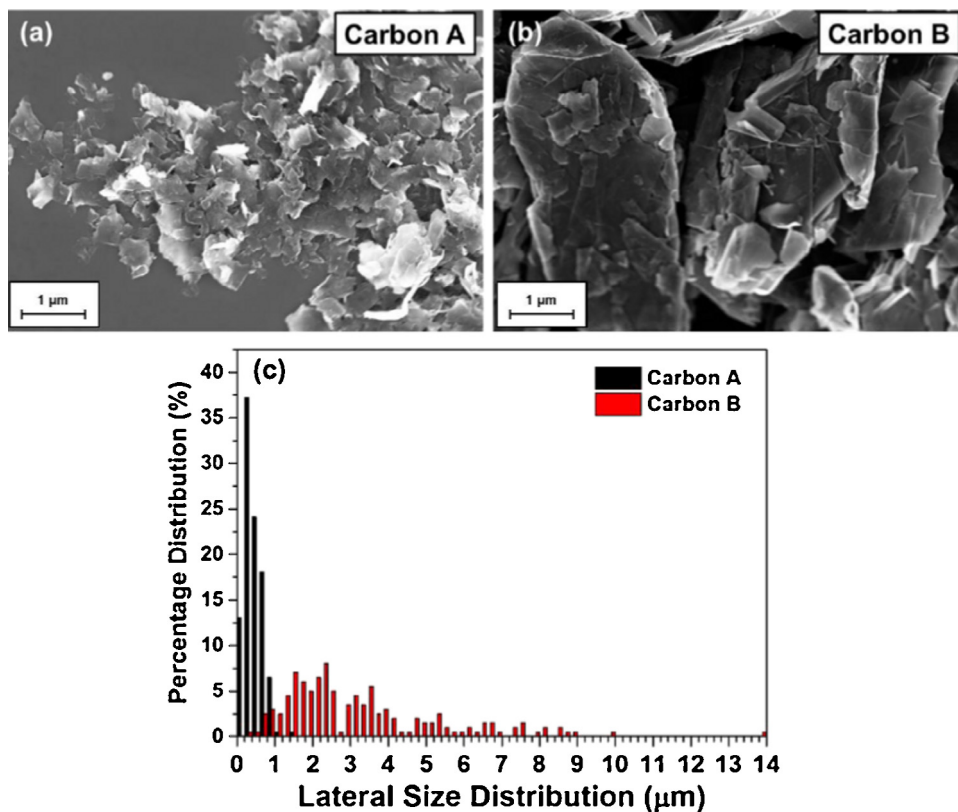
Fig. 2. Flake lateral size: SEM of flakes from Carbon A (a) and Carbon B (b) powders deposited onto a silicon wafer, showing significant variation in flake size and (c) histogram of lateral size distributions of 200 individual flakes from each powder.
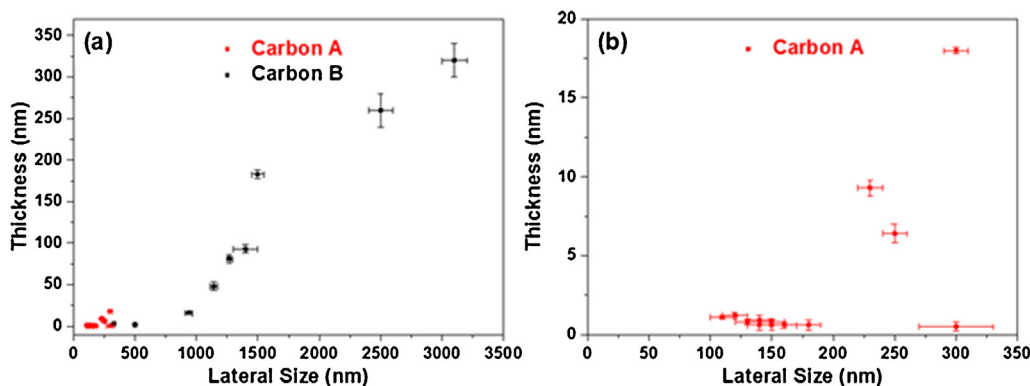

Fig. 3. Flake thickness vs lateral size: Lateral size and thickness correlation of flakes from (a) Carbon A and Carbon B measured using AFM, with a rescaled plot of Carbon A shown in (b) highlighting the variation in thickness between the two samples.

binding energy position and line-shape revealed upon peak fit-ting, there are a few subtle differences evident. The ratio of peak area of the combined carbon-bound oxygen bonding states to the sp^2 peak area from both samples indicates an increased relative concentration of carbon-bound oxygen species for the Carbon A sample [50]. This is coupled with the presence of a small sp^3 peak, which was not observed with the Carbon B material, indicative that another carbon-based material, aside from adventitious carbon due to atmospheric exposure of the powders, is present in the Carbon A material. This correlates with the residue observed on the flakes in the AFM images and Raman spectra. It must be noted that due to the large number of chemical states there is a relatively large associated error expected in the component peak fits. Also, the peak shape of the sp^2 state has an asymmetric nature that is difficult to accurately represent without having a pristine reference spectrum to compare

against. However, even taking this into account, there is a greater concentration of non-graphitic like carbon present in the Carbon A sample. In both cases the same fitting parameters were used, in terms of peak width and asymmetry, with binding energy varia-tions between the component peaks from the two samples allowed only when there was a clear discrepancy between the raw data and the fitted spectra. This manifests itself most clearly in the higher binding energy oxidation states, which are likely due to CO bond-ing with other contaminant elements in the samples (e.g. CO-(Na, S)) [50].

Further, by looking at the total elemental composition of the samples from the XPS spectra, as detailed in Table 1, this variation in composition is reinforced. While the presence of some oxygen is to be expected in these samples due to ex-situ handling and preparation of the pellets, the elevated percentage of oxygen in
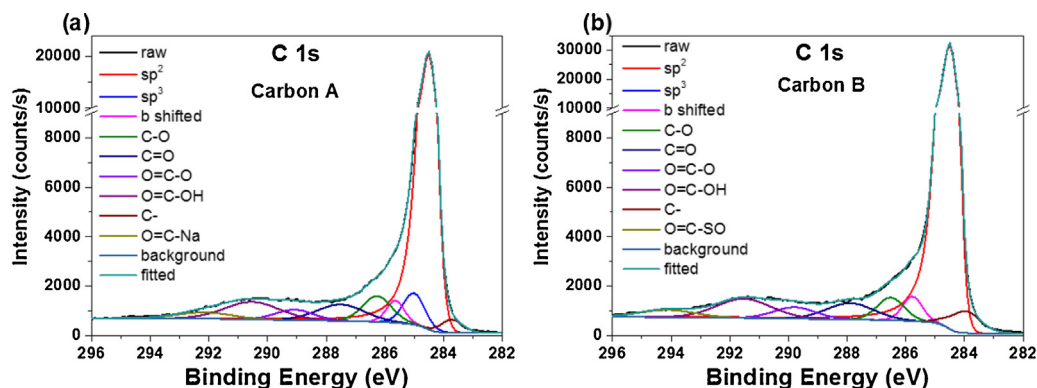
Fig. 4. XPS characterisation of powders: Carbon 1s XPS spectra of (a) Carbon A and (b) Carbon B graphene powders showing variation in concentration of carbon-bound oxygen species present relative to sp²-hybridised carbon, as well as the presence of sp³–hybridised carbon in Carbon A powder. Note that the maximum intensities of the C 1s peaks are different for (a) and (b).

Table 1
Elemental composition of Carbon A and B powders from XPS measurements.

Sample	C%	O%	N%	S%	Ca%	Na%	Fe%
Carbon A	92.5	6.3	0.3	0.0	0.2	0.3	0.2
Carbon B	98.3	1.5	0.0	0.1	0.0	0.0	0.0

the Carbon A sample is greater than would be expected due to this exposure alone. During preparation of the graphene dispersions, it was noted that the Carbon A powder was able to form a more stable dispersion. This is likely due to the presence of a surfactant used in the formation of the powder, which is not fully removed after processing.

From Table 1, there is also clear evidence for the presence of other species in the graphene powders based on the XPS results. While their concentrations are quite low, they are all within the detection limits of the XPS, particularly in the case of Na, N, Ca and Fe being detected in Carbon A, and S detected in Carbon B.

Using this information, XPS was used to attempt to detect the presence of the graphene material in the conductive films. The carbon 1s spectra from the MT46 and PEDOT:PSS films, with and without the addition of Carbon A, representative of both powders are shown in Fig. S4. The spectra from the MT46 and the PEDOT:PSS are virtually identical after the addition of the graphene material, with the only apparent difference being a slight increase in the concentration of C=O bonded carbon. It was not possible to resolve the sp² state due to the graphene in these spectra because of the dominance of the signal from the C—C bonding from the polymers. Also, without complementary sputtering of the sample XPS only probes the first ~10 nm of the surface, this does not provide any information regarding the potential distribution of graphene material in the sample.

In order to determine additional information regarding the extent of contamination present in the graphene, and provide an insight into the distribution of graphene in the films, ToF-SIMS measurements were performed for both the graphene powders and the films produced from printable inks. Fig. 5 shows 250 μm × 250 μm ToF-SIMS surface maps from the same Carbon A and B powder samples used in the XPS and Raman spectroscopy measurements. Polyatomic carbon species (C_n^+, where n > 1) related to graphitic carbon are detected across the whole of the samples as expected, but with a low intensity because of the high bond strength of carbon in this form, and a low ionisation probability of graphitic material. However, adventitious contaminants present on the graphene can have a much higher ion yield allowing femtomole sensitivity.

What is initially evident is that sodium is detected from both samples, but particularly in the case of Carbon A. This correlates

with the XPS data in Table 1. For Carbon A, a large Na signal is detected, co-existent with various CH species, as observed in Fig. 5(a) and (d), indicative of ion peaks coming from a surfactant. Other elements such as Li, Mg, K, Fe, F, I, Br, Ca, S and Cl are also detected.

Through this XPS and ToF-SIMS characterisation of the two carbon materials, it becomes clear that there is a much stronger presence of contaminant species in Carbon A, namely a sodium-containing surfactant. Coupled with the structural characterisation, this would explain why Carbon A shows a large reduction in the resistivity for the non-conductive MT46 film, whilst an increase in resistivity for the conductive PEDOT:PSS film. The larger concentration of thinner graphene flakes in Carbon A must form a percolation network within the MT46 composite that is advantageous to reducing the resistivity. However, for a film that is highly-conductive, any conductive benefit of the graphene is offset by the disruption to the PEDOT:PSS film due to the chemical contamination present. To confirm this, how well Carbon A and Carbon B disperse within the two different polymers must be determined.

Clearly any attempt to differentiate graphene (C_n ions) directly from a polymer matrix with high carbon content is difficult with ToF-SIMS. However, the localisation of graphene could be inferred using novel data analysis of the sodium intensity, with ppm sensitivity, due to the adventitious contamination observed in the powders. The sodium intensity for Carbon A and B provides a sufficient signal-to-noise ratio to allow a lateral ToF-SIMS imaging resolution up to 500 nm.

Depth profiling of polymers is achieved by sputtering the sample with an argon gas cluster ion beam. These ions efficiently remove material without retained sub-surface damage. This works excellently for all polymers [51]. However, a complication occurs when graphitic carbon is added to the polymer since the sputtering rates vary by three orders of magnitude [52]. This results in graphene flakes effectively shielding the polymer material below and essentially a 'pile-up' effect of graphitic material will take place. Consequently, interpretation of the 3D images needs to be done with care. Also, depending on the density of graphene material present, this can prevent the acquisition of a signal from the substrate (in this case aluminium foil), and makes it difficult to accurately locate the interface with the substrate in the ToF-SIMS profiles.

However, from comparison of the Na⁺ ion signal from a graphene-free MT46 sample with MT46 samples containing Carbon A and Carbon B, as shown in Fig. 6(a), it is observed that while there is no obvious sodium signal detected from the bare polymer over the total sputtered depth, with the addition of either of the
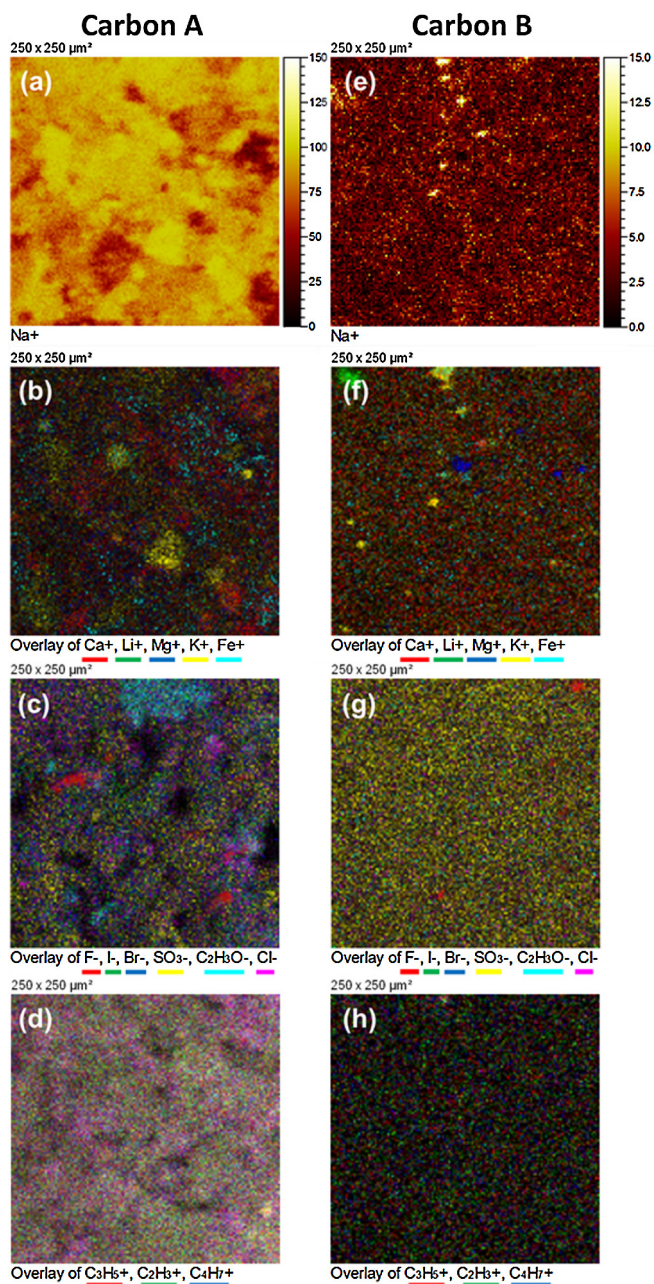
Carbon A

Carbon B

Fig. 5. SIMS characterisation of powders: ToF-SIMS images of (a–d) Carbon A and (e–h) Carbon B powders indicating the detection of various chemical species present in the powders, with (d) in particular highlighting the presence of a surfactant material in Carbon A that is not observed for Carbon B.

two graphene materials, there is an appreciable signal detected. The greater relative Na$^+$ signal observed for Carbon A in Fig. 5(a) when compared to Carbon B in Fig. 5(e), is also shown in the depth profiles from the MT46 samples in Fig. 6(a), and is revealed to decrease with increasing sputter depth. The Na$^+$ signal does not reduce to zero possibly due to the pile-up effect, discussed previously.

Unlike MT46, with PEDOT:PSS a significant sodium signal is already present in the polymer material, as the SO$_3$H component of the polystyrene sulfonate is strongly acidic and leads to the production of various salts of the polymer to form the conductive ionomer. For this reason Na, Ca, Al and Fe were readily detected in the 'PEDOT:PSS only' polymers. However, as shown in Fig. 6(b), the addition of graphene material leads to an increased sodium signal over the baseline detected from a graphene-free sample.

To better understand to what extent the aqueous polymer material could be contributing to the distribution of the Na signal in the film through 'washing' of the surfactant or Na residue from the powder, a sample of the same Carbon A powder used in the previous ToF-SIMS and XPS measurements underwent an intentional rigorous washing process in water, and was subsequently re-examined with ToF-SIMS. The Na signal was observed to decrease by an order of magnitude, as indicated in Fig. S5, but still retained a concentration greater than that observed for Carbon B. This indicates that there is likely to be a redistribution of the Na signal throughout the film as a result of addition to the binder, and may explain the increased signal close to the sample surface during the depth profile in Fig. 6(a).

However, to determine whether the Na signal can still be used to identify the presence and distribution of the carbon materials in the films, a transparent Carbon B/MT46 film (containing a lower concentration of graphene in the printable ink and deposited onto PET to aid transparency) was mapped by optical microscopy, with ToF-SIMS depth profiling subsequently carried out on the same area of the sample, as shown in Fig. 6(c) and (d) respectively. By correlating the optical image directly to the ion image, we observe that regions with a higher Na$^+$ ion signal correspond to the areas where agglomerated graphitic material are present.

Using this information, ToF-SIMS images were produced showing the lateral distribution of the Na$^+$ ion signal from both carbon materials over an analysed region (150 μm × 150 μm) in the MT46 or PEDOT:PSS binders, and a variation in the location of the Na signal clearly is evident using the two different carbon powders. Fig. 7(a) and (c) show the Na$^+$ (red) and Al$^+$ (green) signals overlaid from the Carbon A and B samples in MT46, with Fig. 7(b) and (d) showing the images from the PEDOT:PSS samples. The colour contrast between the MT46 and PEDOT:PSS samples is primarily due to the relative increase in the Na signal in the PEDOT:PSS samples.

With the Carbon A powder, in both cases, we observe a relatively uniform Na distribution, with few obvious areas of variation in signal intensity. The emergence of a substrate Al$^+$ ion signal with increasing sputter depth is greatly limited by the extensive coverage of graphene material over the sputtered area, with signal only detected in random small locations. This indicates that the graphene powder is laterally well distributed in the layer. However, with Carbon B, upon sputtering, a much stronger Al$^+$ ion signal is detected with increasing sputter depth, with large areas of Al$^+$ signal observed to open up amongst apparent 'islands' of Na$^+$ signal. This is indicating that graphene material has agglomerated in these regions of high Na signal intensity, consistent with the ToF-SIMS measurements of the transparent sample, shown in Fig. 6(d). The emergence of the substrate Al signal in the PEDOT:PSS samples is less obvious than with the MT46 samples, possibly due to a better dispersion of carbon material in these samples, but the complications due to the presence of both Na and Al ion signals coming from the PEDOT:PSS material itself should also be taken into account. Even considering this, a clear difference between the dispersion of Carbon A and Carbon B within the polymers is observed.

It is difficult to optically discern differences between the graphene material distribution in these samples, as shown in Fig. S6, due to the opaque Al foil substrate and the greater graphene powder concentration relative to the sample used in Fig. 6(c), however, these ToF-SIMS images indicate that ToF-SIMS is a powerful technique for aiding in identifying the distribution characteristics of the carbon material in films. To further confirm that graphene material was distributed throughout the films, Raman spectroscopy mapping was carried out on the Carbon A in MT46 sample, as shown in Fig. S7. A graphitic signal (G- and 2D-peak) was detected uniformly across the sample, indicating the presence of graphene throughout the film, consistent with the ToF-SIMS data interpretation of this sample.
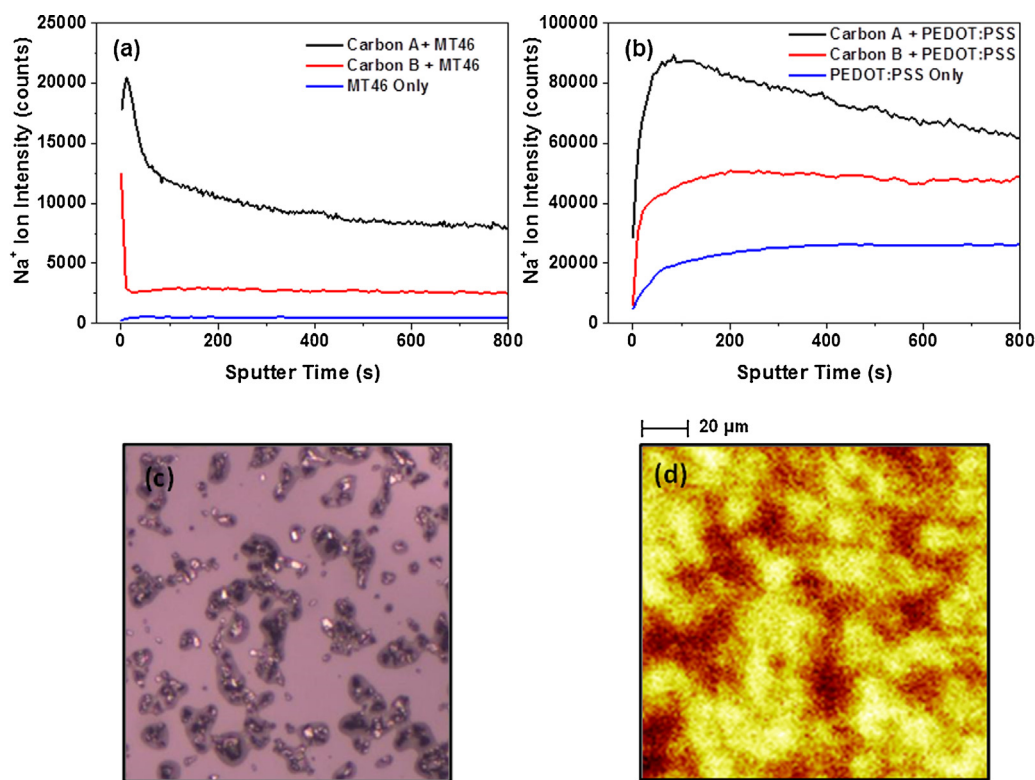
Fig. 6. Chemical characterisation of films: ToF-SIMS depth profiles of polymer samples showing the depth distribution of Na+ signal from Carbon A and B, as well as from the graphene-free polymer, indicating increased Na signal with the addition of graphene, for (a) MT46 samples and (b) PEDOT:PSS samples. (c) Optical image (20×) of Carbon B in MT46 polymer binder deposited on a transparent PET substrate indicating agglomeration of graphitic material in locations dispersed across the sample. The corresponding Na+ ToF-SIMS image (150 μm × 150 μm) from the same location during ToF-SIMS depth profiling is shown in (d) indicating an enhancement of the Na signal in the same regions where the graphitic material is observed in the optical image.

ToF-SIMS analysis of the sodium signal therefore reveals that Carbon A does indeed disperse within the two different polymers, whilst the introduction of Carbon B leads to the agglomeration of graphitic material within the composite. This would concur with the comprehensive structural characterisation that shows Carbon A contains a much greater concentration of thinner, smaller graphene flakes than Carbon B. This leads to the reduction in resistivity observed for Carbon A when introduced to the non-conductive MT46 polymer, due to the formation of a percolation network. Meanwhile, the increase in resistivity observed for the PEDOT:PSS and Carbon A composite can be explained due to the presence of a non-conductive surfactant disrupting the highly-conductive polymer film, even if there is an apparent improvement in material distribution for Carbon A in PEDOT:PSS when compared to Carbon B. This shows that understanding both the physical and chemical properties of graphene material is necessary for any potential benefit, in this case for conductive polymer films produced from printable inks, to be fully realised.

4. Conclusions

A range of complementary characterisation techniques have been employed to determine the physical and chemical properties of graphene powders before and after inclusion in polymers, with the aim of creating conductive films from printable inks. Thickness and lateral dimension analysis highlight that the size distribution of flakes can vary significantly from supplier to supplier, and also that the chemical properties of these powders can be quite different. Elemental contaminants have been identified, through the use of XPS and ToF-SIMS measurements, as being present in the graphene powders, leading to questions regarding unexpected doping or con-

sistency of material properties, warranting further studies. These differences are shown to directly affect the electrical properties of graphene-polymer composites when these commercial samples are combined with polymers such as an insulating acrylic binder or the already conductive PEDOT:PSS. Improved material distribution can be achieved with graphene powders containing a greater concentration of thinner, laterally-smaller flakes that ultimately reduce the resistivity of the graphene-polymer composite films. However, chemical contamination of the graphene material can cause an increase in the resistivity of the films when using a highly-conductive polymer.

ToF-SIMS depth profiling of films containing these powders was performed and while it is difficult to directly measure signal from the graphitic material, by tracking the signal from contaminant species such as sodium, it is possible to generate a picture of the distribution profile of the graphene material in the films and explore how well it is distributed. This technique can map areas hundreds of microns in size, be used for films that do not show any variation optically and without the requirement for extensive sample preparation.

This study highlights the effectiveness of using multiple complementary microscopy and spectroscopy techniques to aid in the further understanding and improvement of graphene-enhanced devices, as well as the need for adequate characterisation data to enable the emerging graphene industry. Also of note is that although the material properties revealed by the characterisation of the commercially-available graphene materials show similarities to the material specifications of the suppliers, there is variation. This study shows that the measurement uncertainties are not fully understood and thus interlaboratory comparisons are desperately required to enable the graphene market. As there is not
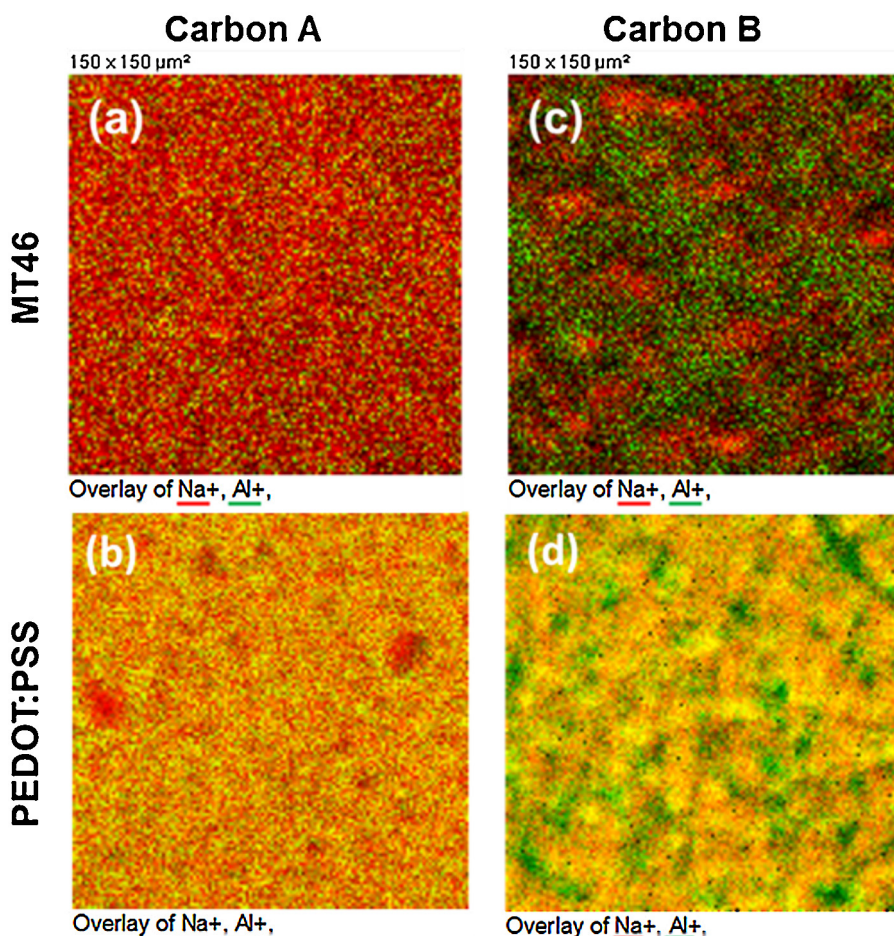
Fig. 7. Mapping of flake dispersion within the polymer: ToF-SIMS images of the Na$^+$ (red) and Al$^+$ (green) ion signals during 3D depth profiling from (a and b) Carbon A and (c and d) Carbon B in MT46 or PEDOT:PSS on Al foil. The emergence of the Al signal is observed with increasing sputter depth, and in the case of the Carbon B samples, indicates there are regions of graphene material agglomeration, whereas with Carbon A, a more uniform distribution of material in the binders is observed. (For interpretation of the references to colour in this figure legend, the reader is referred to the web version of this article.)

yet an accepted set of protocols for the structural characterisation of graphene powders, this work can be used as a base for future international interlaboratory comparisons through the VAMAS framework, supporting the international standardisation work already initiated within ISO/TC229.

Appendix A. Supplementary data

Supplementary data associated with this article can be found, in the online version, at http://dx.doi.org/10.1016/j.apsusc.2017.01.132.

References

[1] A.C. Ferrari, F. Bonaccorso, V. Fal'ko, K.S. Novoselov, S. Roche, P. Bøggild, et al., Science and technology roadmap for graphene, related two-dimensional crystals, and hybrid systems, Nanoscale 7 (2015) 4598.

[2] F. Withers, H. Yang, L. Britnell, A.P. Rooney, E. Lewis, A. Felten, et al., Heterostructures produced from nanosheet-based inks, Nano Lett. 14 (2014) 3987–3992.

[3] T. Georgiou, R. Jalil, B.D. Belle, L. Britnell, R.V. Gorbachev, S.V. Morozov, et al., Vertical field-effect transistor based on graphene-WS2 heterostructures for flexible and transparent electronics, Nat. Nanotechnol. 8 (2013) 100–103.

[4] A.V. Kretinin, Y. Cao, J.S. Tu, G.L. Yu, R. Jalil, K.S. Novoselov, et al., Electronic properties of graphene encapsulated with different two-dimensional atomic crystals, Nano Lett. 14 (2014) 3270–3276.

[5] Z. Liu, K. Parvez, R. Li, R. Dong, X. Feng, K. Müllen, Transparent conductive electrodes from Graphene/PEDOT:PSS hybrid inks for ultrathin organic photodetectors, Adv. Mater. 27 (2015) 669–675.

[6] K.S. Novoselov, V.I. Falko, L. Colombo, P.R. Gellert, M.G. Schwab, K. Kim, A roadmap for graphene, Nature 490 (2012) 192–200.

[7] F. Bonaccorso, Z. Sun, T. Hasan, A.C. Ferrari, Graphene photonics and optoelectronics, Nat. Photon. 4 (2010) 611–622.

[8] P. Matyba, H. Yamaguchi, G. Eda, M. Chhowalla, L. Edman, N.D. Robinson, Graphene and mobile ions: the key to all-plastic solution-processed light-emitting devices, ACS Nano 4 (2010) 637–642.

[9] A.D. Smith, K. Elgammal, F. Niklaus, A. Delin, A.C. Fischer, S. Vaziri, et al., Resistive graphene humidity sensors with rapid and direct electrical readout, Nanoscale 7 (2015) 19099–19109.

[10] P. Samorì, I.A. Kinloch, X. Feng, V. Palermo, Graphene-based nanocomposites for structural and functional applications: using 2-dimensional materials in a 3-dimensional world, 2D Mater. 2 (2015) 030205.

[11] F. Bonaccorso, L. Colombo, G. Yu, M. Stoller, V. Tozzini, A.C. Ferrari, et al., Graphene, related two-dimensional crystals, and hybrid systems for energy conversion and storage, Science 347 (2015) 1246501.

[12] Y. Zhu, S. Murali, M.D. Stoller, K.J. Ganesh, W. Cai, P.J. Ferreira, et al., Carbon-based supercapacitors produced by activation of graphene, Science 332 (2011) 1537–1541.

[13] N. Shang, P. Papakonstantinou, P. Wang, S.R.P. Silva, Platinum integrated graphene for methanol fuel cells, J. Phys. Chem. C 114 (2010) 15837–15841.

[14] J.V. Anguita, M. Ahmad, S. Haq, J. Allam, S.R.P. Silva, Ultra-broadband light trapping using nanotextured decoupled graphene multilayers, Sci. Adv. 2 (2016).

[15] Y.Y. Tan, K.D.G.I. Jayawardena, A.A.D.T. Adikaari, L.W. Tan, J.V. Anguita, S.J. Henley, et al., Photo-thermal chemical vapor deposition growth of graphene, Carbon 50 (2012) 668–673.

[16] M.-B. Martin, B. Dlubak, R.S. Weatherup, M. Piquemal-Banci, H. Yang, R. Blume, et al., Protecting nickel with graphene spin-filtering membranes: a single layer is enough, Appl. Phys. Lett. 107 (2015) 012408.

[17] F. Xia, D.B. Farmer, Y.-M. Lin, P. Avouris, Graphene field-effect transistors with high on/off current ratio and large transport band gap at room temperature, Nano Lett. 10 (2010) 715–718.

[18] T.J.B.M. Janssen, S. Rozhko, I. Antonov, A. Tzalenchuk, J.M. Williams, Z. Melhem, et al., Operation of graphene quantum Hall resistance standard in a cryogen-free table-top system, 2D Mater. 2 (2015) 035015.

[19] J.R. Potts, D.R. Dreyer, C.W. Bielawski, R.S. Ruoff, Graphene-based polymer nanocomposites, Polymer 52 (2011) 5–25.

[20] Z. Zhu, J. Chen, Review—advanced carbon-supported organic electrode materials for lithium (sodium)-ion batteries, J. Electrochem. Soc. 162 (2015) A2393–A2405.

[21] J. Hassoun, F. Bonaccorso, M. Agostini, M. Angelucci, M.G. Betti, R. Cingolani, et al., An advanced lithium-ion battery based on a graphene anode and a lithium iron phosphate cathode, Nano Lett. 14 (2014) 4901–4906.

[22] H.A. Becerril, J. Mao, Z. Liu, R.M. Stoltenberg, Z. Bao, Y. Chen, Evaluation of solution-Processed reduced graphene oxide films as transparent conductors, ACS Nano 2 (2008) 463–470.

[23] K. Ghaffarzadeh, R. Das, Transparent conductive films (TCF) 2015–2025: forecasts, markets, technologies, IDTechEx (2015).

[24] E.B. Secor, P.L. Prabhumirashi, K. Puntambekar, M.L. Geier, M.C. Hersam, Inkjet printing of high conductivity, flexible graphene patterns, J. Phys. Chem. Lett. 4 (2013) 1347–1351.

[25] V. Babenko, A.T. Murdock, A.A. Koos, J. Britton, A. Crossley, P. Holdway, et al., Rapid epitaxy-free graphene synthesis on silicidated polycrystalline platinum, Nat. Commun. 6 (2015).

[26] A. Pirkle, J. Chan, A. Venugopal, D. Hinojos, C.W. Magnuson, S. McDonnell, et al., The effect of chemical residues on the physical and electrical properties of chemical vapor deposited graphene transferred to SiO2, Appl. Phys. Lett. 99 (2011) 122108.

[27] G.H. Wells, M.R.C. Hunt, T. Hopf, K.V. Vassilevski, E. Escobedo-Cousin, A.B. Horsfall, et al., Facile technique for the removal of metal contamination from graphene, J. Vac. Sci. Technol. B 33 (2015) 051802.

[28] M.J. Allen, V.C. Tung, R.B. Kaner, Honeycomb carbon: a review of graphene, Chem. Rev. 110 (2010) 132–145.

[29] A. Bianco, H.-M. Cheng, T. Enoki, Y. Gogotsi, R.H. Hurt, N. Koratkar, et al., All in the graphene family – a recommended nomenclature for two-dimensional carbon materials, Carbon 65 (2013) 1–6.

[30] X. Li, W. Cai, J. An, S. Kim, J. Nah, D. Yang, et al., Large-area synthesis of high-quality and uniform graphene films on copper foils, Science 342 (2009) 1312–1314.

[31] A.N. Obraztsov, Chemical vapour deposition: making graphene on a large scale, Nat. Nanotechnol. 4 (2009) 212–213.

[32] R.S. Weatherup, B. Dlubak, S. Hofmann, Kinetic control of catalytic CVD for high-quality graphene at low temperatures, ACS Nano 6 (2012) 9996–10003.

[33] I. Vlassiouk, P. Fulvio, H. Meyer, N. Lavrik, S. Dai, P. Datskos, et al., Large scale atmospheric pressure chemical vapor deposition of graphene, Carbon 54 (2013) 58–67.

[34] D. Li, M.B. Muller, S. Gilje, R.B. Kaner, G.G. Wallace, Processable aqueous dispersions of graphene nanosheets, Nat. Nanotechnol. 3 (2008) 101–105.

[35] A. Ambrosi, C.K. Chua, B. Khezri, Z. Sofer, R.D. Webster, M. Pumera, Chemically reduced graphene contains inherent metallic impurities present in parent natural and synthetic graphite, Proc. Nat. Acad. Sci. U. S. A. 109 (2012) 12899–12904.

[36] L. Huang, Y. Huang, J. Liang, X. Wan, Y. Chen, Graphene-based conducting inks for direct inkjet printing of flexible conductive patterns and their applications in electric circuits and chemical sensors, Nano Res. 4 (2011) 675–684.

[37] L. Wan, B. Wang, S.M. Wang, X.B. Wang, Z.G. Guo, B.H. Dong, et al., Well-dispersed PEDOT:PSS/graphene nanocomposites synthesized by in situ polymerization as counter electrodes for dye-sensitized solar cells, J. Mater. Sci. 50 (2015) 2148–2157.

[38] W.K. Chee, H.N. Lim, N.M. Huang, I. Harrison, Nanocomposites of graphene/polymers: a review, RSC Adv. 5 (2015) 68014–68051.

[39] R. Giardi, S. Porro, A. Chiolerio, E. Celasco, M. Sangermano, Inkjet printed acrylic formulations based on UV-reduced graphene oxide nanocomposites, J. Mater. Sci. 48 (2013) 1249–1255.

[40] A. Chiolerio, S. Porro, S. Bocchini, Impedance hyperbolicity in inkjet-printed graphene nanocomposites: tunable capacitors for advanced devices, Adv. Electron. Mater. 2 (2016) 1500312.

[41] M.P. Seah, I.S. Gilmore, S.J. Spencer, Quantitative XPS: I. Analysis of X-ray photoelectron intensities from elemental data in a digital photoelectron database, J. Electron Spectrosc. 120 (2001) 93–111.

[42] K.R. Paton, E. Varrla, C. Backes, R.J. Smith, U. Khan, A. O'Neill, et al., Scalable production of large quantities of defect-free few-layer graphene by shear exfoliation in liquids, Nat. Mater. 13 (2014) 624–630.

[43] M.M. Lucchese, F. Stavale, E.H. Martins Ferreira, C. Vilani, M.V.O. Moutinho, R.B. Capaz, et al., Quantifying ion-induced defects and Raman relaxation length in graphene, Carbon 48 (2010) 1592–1597.

[44] A.J. Pollard, B. Brennan, H. Stec, B.J. Tyler, M.P. Seah, I.S. Gilmore, et al., Quantitative characterization of defect size in graphene using Raman spectroscopy, App. Phys. Lett. 106 (2014) 253107.

[45] S. Mignuzzi, N. Kumar, B. Brennan, I.S. Gilmore, D. Richards, A.J. Pollard, et al., Probing individual point defects in graphene via near-field Raman scattering, Nanoscale 7 (2015) 19413–19418.

[46] Y. Shin, E. Prestat, K.-G. Zhou, P. Gorgojo, K. Althumayri, W. Harrison, et al., Synthesis and characterization of composite membranes made of graphene and polymers of intrinsic microporosity, Carbon 102 (2016) 357–366.

[47] C. Casiraghi, A. Hartschuh, H. Qian, S. Piscanec, C. Georgi, A. Fasoli, et al., Raman spectroscopy of graphene edges, Nano Lett. 9 (2009) 1433–1441.

[48] R. Beams, L. Cancado, L. Novotny, Raman characterization of defects and dopants in graphene, J. Phys. Condens. Matter 27 (2015) 083002.

[49] E. Varrla, C. Backes, K.R. Paton, A. Harvey, Z. Gholamvand, J. McCauley, et al., Large-scale production of size-controlled MoS2 nanosheets by shear exfoliation, Chem. Mat. 27 (2015) 1129–1139.

[50] U. Gelius, P.F. Heden, J. Hedman, B.J. Lindberg, R. Manne, R. Nordberg, et al., Molecular spectroscopy by means of ESCA. III. Carbon compounds, Phys. Scr. 2 (1970) 70.

[51] B.J. Tyler, B. Brennan, H. Stec, T. Patel, L. Hao, I.S. Gilmore, et al., Removal of organic contamination from graphene with a controllable mass-selected argon gas cluster ion beam, J. Phys. Chem. C 119 (2015) 17836–17841.

[52] M.P. Seah, Universal equation for argon gas cluster sputtering yields, J. Phys. Chem. C 117 (2013) 12622.